





Collisions of micron-sized charged water droplets in still air

G. Magnusson ¹, A. Dubey ¹, R. Kearney ², G. P. Bewley,² and B. Mehlig ¹

¹*Department of Physics, Gothenburg University, 41296 Gothenburg, Sweden*

²*Sibley School of Mechanical and Aerospace Engineering, Cornell University, Ithaca, 14853 New York, USA*



(Received 22 June 2021; accepted 16 February 2022; published 4 April 2022)

We show that the relative dynamics of charged water droplets settling in still air contains fixed points determined by the combination of hydrodynamic interactions, particle and fluid inertia, and electrostatic forces. For droplets with large enough opposite charges, the stable manifold of a saddle forms a separatrix that divides colliding trajectories from those that do not collide. We analyzed experimental data of hydrodynamically interacting, micron-sized water droplets in still air with Lagrangian droplet tracking and with a numerical model including gravity, particle inertia, hydrodynamic interactions, fluid inertia, and Coulomb interactions. The predictions of the model are in excellent agreement with the experiments. A consequence of our findings is that, for large charges, collision outcomes are not sensitive to the breakdown of hydrodynamics at small distances.

DOI: [10.1103/PhysRevFluids.7.043601](https://doi.org/10.1103/PhysRevFluids.7.043601)

I. INTRODUCTION

The collision-driven growth of small water droplets in air is of great importance in atmospheric physics [1]. Cloud droplets tend to carry charges in thunderclouds but also in warm rain clouds [2], and the resulting electrostatic forces affect droplet-collision rates and thus the droplet-size distribution. The collision dynamics of charged cloud droplets has been studied by numerical integration of model equations. But it is not known when these models work, how they fail, and how Coulomb forces compete with hydrodynamic effects to determine the rate at which charged droplets settling through a cloud grow by collision. Even for still air, in the absence of cloud turbulence, there is no theory explaining the parametric dependence upon charge, droplet size, and velocity.

Several mechanisms affect droplet collisions between neutral droplets settling in a quiescent fluid. Hydrodynamic interactions bend the path of one droplet around a second one [Fig. 1(a)], reducing their chance of colliding. Particle inertia may cause droplets of different sizes to collide nevertheless, because it allows them to detach from the streamlines of the flow [3,4]. Yet this mechanism does not allow equally sized droplets to approach in the creeping-flow limit, a consequence of time-reversal symmetry. Fluid inertia breaks this symmetry and enables droplets of the same size to approach, as shown by Klett and Davis [5]. However, their approximation of the hydrodynamic interactions fails as the droplets approach. Early experiments [6] designed to check the theory of Klett and Davis [5] are inconclusive because they used an updraft to keep the droplets within the field of vision of the cameras, with unclear consequences [7,8]. More fundamentally, Klett and Davis [5] did not consider how the hydrodynamic approximation breaks down below the mean free path. This is important because this effect regularizes an artificial singularity of the hydrodynamic force [9,10], which would otherwise prevent droplets from colliding.

Published by the American Physical Society under the terms of the [Creative Commons Attribution 4.0 International](https://creativecommons.org/licenses/by/4.0/) license. Further distribution of this work must maintain attribution to the author(s) and the published article's title, journal citation, and DOI. Funded by [Bibsam](https://www.bibsam.com/).

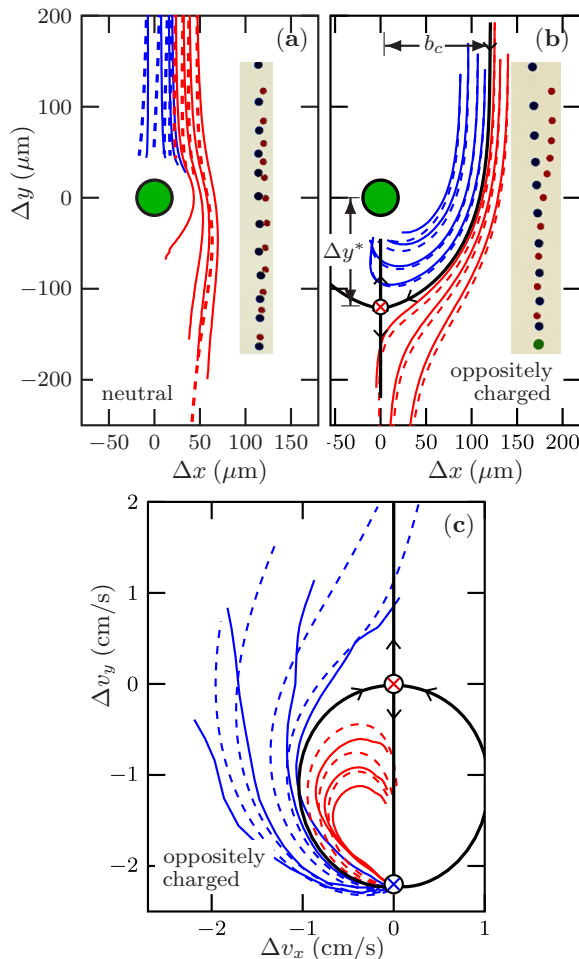


FIG. 1. (a) Spatial separation of neutral droplets in the rest frame of the smaller droplet (green disk). Experiments (solid lines) and fitted simulations of Eqs. (1) (dashed lines). Blue lines indicate that the experiment resulted in a collision, red lines a miss. The inset shows false-color snapshots from the video recording of two noncolliding trajectories. (b) Same but for oppositely charged droplets. The inset shows two colliding trajectories. The red encircled cross indicates the location of a saddle point (see text) at $(0, \Delta y^*)$, together with its stable and unstable manifolds (solid black lines). As $t \rightarrow -\infty$, the stable manifold connects to an unstable fixed point at (∞, b_c) . (c) Relative velocities for charged droplets. The blue encircled cross indicates the fixed point at infinity.

Coulomb interactions compete with hydrodynamic effects, particle inertia, and fluid inertia. The effects of charge on droplet collisions is understood on a rudimentary level: opposite charges increase collision efficiencies, and charges are more important for smaller droplets than for larger ones [1,2]. Davis [11] finds that more than 800 elementary charges are needed for the Coulomb force to noticeably change the collision efficiency for $20 \mu\text{m}$ droplets, the typical size of cloud droplets, but Tinsley and Zhou [12] state that at least 10 000 elementary charges are required. Semonin and Plumlee [13] quote a limit of 6000 elementary charges.

Early model calculations could not resolve these discrepancies because they neglected hydrodynamic interactions and fluid inertia [14], causing the model to break down for realistic charges [15]. More recent model calculations [16,17] contained hydrodynamic interactions, but only ap-

proximately [5]. It is not known whether the model works, even qualitatively, or not. In addition, these numerical studies were restricted to selected droplet radii and charges, and could therefore not resolve the uncertainties mentioned above. More importantly, a lack of experimental data makes it impossible to validate the models, even for droplet collisions in still air.

We therefore investigated the collision dynamics of water droplets settling in still air, using Lagrangian tracking [18] to analyze experimental data on collisions of charged water droplets in still air. The data were collected with a setup similar to that described in Hanstorp *et al.* [19]. We explain the observed collision dynamics [Figs. 1(b) and 1(c)] by characterizing its fixed points and their invariant manifolds. Our analysis describes how the collision dynamics depends on droplet charges and radii, amongst other parameters. The theory is accurate for the charges we consider. We discuss how it breaks down for smaller charges.

II. BACKGROUND

Figure 1 shows two components of the spatial separation between two settling droplets, Δx and Δy , in the rest frame of the smaller droplet. Gravity points downwards. Whether the droplets collide is determined by the impact parameter b , the Δx coordinate at $\Delta y = \infty$. The collision efficiency is defined as $b_c^2/(a_1 + a_2)^2$ [1], where b_c is the impact parameter of the grazing path, and a_1 and a_2 are the droplet radii. The motion of a single water droplet in still air is controlled by three non-dimensional numbers: St , Re_p , and Sl . The Stokes number $St = (\tau_c \gamma)^{-1}$ compares the particle relaxation time γ^{-1} to τ_c , the characteristic acceleration timescale due to electrical charges on the droplets, $\tau_c = \sqrt{a/\alpha_c}$, where α_c is the Coulomb acceleration upon contact. The Stokes constant is $\gamma = 9\rho_f v / (2a^2 \rho_p)$ with fluid-mass density ρ_f , kinematic viscosity ν , droplet radius a , and droplet-mass density ρ_p . Fluid inertia resists the motion of the surrounding air that moves along with the droplet. This effect is quantified by the particle Reynolds number $Re_p = av/\nu$, where v is the relative speed between the droplet and the air. An accelerating droplet accelerates the surrounding air. The magnitude of this unsteady effect is quantified by the Strouhal number, $Sl = a/(v\tau_c)$.

In the presence of a second droplet, a fourth non-dimensional number a/R (center-to-center distance R between the droplets) determines the strength of hydrodynamic interactions between the droplets, which can be computed as a perturbation expansion in a/R . In the creeping-flow limit, this corresponds to the method of reflections [9]. As mentioned above, fluid inertia becomes important for similar-sized droplets. One can account for this effect by perturbation theory in Re_p [20]. A fifth parameter, the Knudsen number Kn , is defined as the ratio of the mean free path of air to the droplet radius. For neutral droplets, the breakdown of hydrodynamics must be considered at small interfacial separations $s \equiv R - (a_1 + a_2)$, when s/a is of the order of Kn or smaller [10].

The Coulomb number, Cu , is commonly used to quantify the effect of electrical charges on the droplet dynamics. This nondimensional parameter is defined as $Cu = |E_C|/E_{kin}$, where $E_C = k_e q_1 q_2 / (a_1 + a_2)$ is the Coulomb energy upon impact (Coulomb constant k_e , droplet charges q_1 and q_2 , and droplet radii a_1 and a_2), and E_{kin} is the kinetic energy based on the initial relative velocity. Defined in this way, Cu parametrizes the critical collision efficiency for the central-force problem [21], without dissipation or hydrodynamical interactions. The definition is analogous to the non-dimensional number used to quantify the effect of electric charge on coagulation in Brownian suspensions [22]. Lu *et al.* [23–25] define an analogous parameter to describe the effect of charge on spatial clustering of droplets in turbulence.

III. METHODS

A. Experimental data

The measurements reported here were taken using a setup similar to the one described by Hanstorp *et al.* [19]. For details, see Appendix A. Droplets between 17 and 25 μm in radius were generated using inkjet-printer nozzles [26]. The oppositely charged droplets carried about

10^5 elementary charges. The neutral droplets had less than 2500 elementary charges per droplet. Two nozzles were angled so that collisions and near-collisions could be observed simultaneously by two high-speed cameras. Electrical charge was imparted to the droplets by applying a DC voltage to an electrode near the dispenser nozzle [19]. The resulting charge-per-mass ratio was measured separately by allowing single droplets to fall between two parallel charged conducting plates.

B. Tracking

We estimated the radii and positions of droplets using the circle-fitting method of Pratt [27] as described by Kearney and Bewley [18]. They tested this method on synthetic data similar to the present experimental data, and demonstrated that the algorithm outperforms other methods in measuring the sizes and positions of droplets in high resolution, in particular when the droplet images overlap in the camera plane.

We tracked the droplets separately in each camera plane using the hybrid method discussed in Ref. [18]. The internal clocks of the two cameras were not synchronized, therefore we determined the time delay between the cameras using the moment of collision as a reference. We excluded any video recordings in which no collisions occurred. We reconstructed the three-dimensional trajectories assuming the optical axes of the cameras were orthogonal, taking the x and y - coordinates from one camera and the z coordinates from the other one. The uncertainty in finding the droplet positions in the digital images was less than half a pixel [18] or about $0.9 \mu\text{m}$.

Droplet radii were measured using images from camera 1, collinear with the z axis, because the images recorded by camera 2 were not uniformly illuminated, causing a bias in the measured droplet sizes. We found that the minimum of the time signal of measured droplet radius along a trajectory corresponded to the image frame which was in best focus. However, we used the 10th percentile of the signal, instead of the minimum, as our estimate for the true droplet size because it is robust to noise [28]. The radii thus measured contained a systematic error that we corrected by estimating bounds on the radii using information near collisions. An upper bound for the sum of the radii is the minimum separation distance immediately prior to collision plus the uncertainty in finding the droplet positions, mentioned above. A lower bound is given by the predicted separation distance in one time step (using the velocity estimates at the end of each trajectory, described below) minus the uncertainty in the droplet positions. The mean of these two bounds agreed well with the radii of the droplets measured directly from camera 1 once a correction factor of 0.85 was applied. This correction factor is required for two reasons, both of which lead to an increase in the estimated droplet size. First, a Gaussian blur in the droplet-identification algorithm leads to an overestimate of the droplet size. Second, diffraction patterns increase the perceived droplet size.

Droplet velocities were calculated using a two-point, forward finite-difference method and smoothed with a Gaussian filter of window size of either 1 or 0.4 ms, depending on the frame rate of the cameras. This filter size was large enough that it reduced the effect of noise due to uncertainty in the droplet positions, but it was smaller than the relaxation time of the droplets. We discarded short trajectories (fewer than ten data points) that were more likely to contain tracking errors.

C. Collision detection

The collision detection method discussed in Ref. [18] cannot be applied to find collisions in the present data because the time it takes two droplets to coalesce into one stable, spherical droplet was longer than the time between each image recorded by the cameras. Instead, in order to determine collision outcome, we used the following three criteria: (1) Two trajectories end (parents) and a new trajectory begins (daughter) within at most 16 frames. (2) The daughter must have a radius equal to the calculated radius that preserves the mass of the parents (within threshold $2 \mu\text{m}$). (3) The daughter may not coexist with any other trajectories. The first criterion provides a permissive threshold for the coalescence time, the time it takes the daughter droplet to achieve a stable spherical shape (rather than oscillating between a prolate and oblate spheroid). The second criterion enforces

conservation of mass when no fragmentation occurs upon collision, which was the case due to the small droplet size [29]. The final criterion prevents a simultaneous interruption in two trajectories from causing a false positive collision detection.

If all the above criteria were fulfilled, we considered a collision to have occurred. If a collision was not found by the criteria above, but the inward component of the relative velocity vector was positive at the final moment of observation, then we marked the event as inconclusive. These were cases in which the collision might or might not have occurred outside the observation volume of the cameras. Otherwise, the event was marked as a miss.

D. Model

In the experiments, droplet Stokes numbers were quite large, in the range $1 < St < 3$, and the Coulomb number was in the range $3 < Cu < 10$. Therefore our model takes into account particle inertia in addition to Coulomb interactions. The equation of motion for droplet j with mass m_j is

$$\dot{\mathbf{x}}^{(j)} = \mathbf{v}^{(j)}, \quad m_j \dot{\mathbf{v}}^{(j)} = \mathbf{F}_g^{(j)} + \mathbf{F}_e^{(j)} + \mathbf{F}_h^{(j)} \quad (1)$$

for $j = 1, 2$. Here $\mathbf{F}_g^{(j)} = m_j \mathbf{g}$ is the gravity force with gravitational acceleration \mathbf{g} . The electrostatic force $\mathbf{F}_e^{(j)}$ is modelled by the Coulomb force $\mathbf{F}_e = k_e q_1 q_2 \mathbf{R} / R^3$, with center-to-center distance vector \mathbf{R} and $R = |\mathbf{R}|$. As a first approximation, we neglect corrections to the Coulomb force due to induced charges [2].

The hydrodynamic force $\mathbf{F}_h^{(j)}$ is computed to linear order in a/R using the method of reflections, taking into account fluid-inertia effects at large separations and for small particle-Reynolds numbers [20]. The method yields an approximate, iterative solution of the Oseen equation using the Green function derived in Ref. [20]. Unsteady effects matter when the Coulomb force causes rapid accelerations. We use the approximate history force for hydrodynamically interacting droplets derived by Ardekani and Rangel [30], and we neglect added-mass effects. The resulting model for the hydrodynamic force for droplet j reads

$$\begin{aligned} \mathbf{F}_h^{(j)} = & -6\pi\mu a_j \left(1 + \frac{3}{8} \frac{a_j v^{(j)}}{\nu}\right) (\mathbf{v}^{(j)} - \mathbf{u}^{(i,j)}) \\ & - 6\pi\mu a_j \int_0^t d\tau \mathbb{K}^{(j)}(t - \tau) \frac{d}{d\tau} \begin{bmatrix} \mathbf{v}^{(1)}(\tau) \\ \mathbf{v}^{(2)}(\tau) \end{bmatrix}. \end{aligned} \quad (2)$$

The first term in Eq. (2) describes the effect of fluid inertia, where $\mathbf{u}^{(i,j)}$ is the disturbance velocity induced at the position of droplet j by droplet i . The droplet-induced velocity field $\mathbf{u}^{(i,j)}$ is calculated to linear order in a/R [20],

$$\begin{aligned} \mathbf{u}^{(i,j)} = & e^{-\frac{1}{2\nu}(v^{(i)}R + v^{(i)} \cdot \mathbf{R})} \frac{\mathbf{f}^{(i)}}{8\pi\mu R} \\ & + \left\{ 1 - \left(1 + \frac{v^{(i)}R}{2\nu}\right) e^{-\frac{1}{2\nu}(v^{(i)}R + v^{(i)} \cdot \mathbf{R})} \right\} \frac{\mathbf{f}^{(i)}}{\rho_f v^{(i)}} \frac{\mathbf{R}}{4\pi R^3}. \end{aligned} \quad (3)$$

Here $\mathbf{f}^{(i)} = 6\pi\nu\rho_f a_i v^{(i)}$ is the force applied by droplet i on the fluid. The second term in Eq. (2) is a history force. The kernel $\mathbb{K}^{(j)}(t - \tau)$ is obtained by expanding the result of Ardekani and Rangel [30] to order a/R , to be consistent with the order of the reflection method considered. Note that Ardekani and Rangel [30] obtained the kernel by solving the unsteady Stokes equation; fluid-inertia corrections to the kernel are not accounted for.

The approximate hydrodynamic force (2) is valid when the droplet separation is much larger than their radii. It fails at small interfacial distances. Previous studies, for instance by Klett and Davis [5] and Schlamp *et al.* [16], used models similar to ours. Klett and Davis [5], for example used the Oseen equation with an *ad hoc* rescaling of the particle Reynolds number, $Re_p \rightarrow Re_p[1 - 0.08 \ln(1 +$

50 Re_p) [1,31], to compute the effect of fluid inertia on small droplet collisions, assuming that the droplet dynamics is two dimensional. In addition, neither our model nor the models in the studies mentioned above account for breakdown of hydrodynamics when the interfacial droplet separation becomes comparable to the mean free path of air, and thus cannot describe collisions of neutral droplets [10].

E. Fitting of experimental data

In this section we discuss the procedure used to fit the model equations, Eq. (1), to the experimental data. Figure 1 shows the experimental and fitted trajectories for two measurements, one with neutral droplet pairs and one with charged droplet pairs. Table I compares the fitted radii and charges to those measured experimentally. While the fitted radii are consistent with the reported radii within error estimates, the fitted charges are smaller than the experimentally reported charges; see Appendix B and Table I. Note that Table I shows the charge squared which has an error about twice as large as the charge magnitudes. In addition, Fig. 4 shows a shift in the distributions of the charge-per-mass even for measurements performed on the same day. We expect the difference between fitted and experimentally observed values, and the shift in charge-per-mass distributions, to be caused by systematic errors in alignment of the web camera used to measure the fall angle of single droplets for determining charge: an upward or downward tilt of the camera would tend to cause an overestimate of the deflection angle. Additionally, it was necessary to clean the dispenser nozzles at regular intervals to prevent clogging, which may have altered the charge imparted to the droplets.

Using droplet radii and charges as fitting parameters, we used least-squares fitting to fit the droplet trajectories obtained by numerical integration of the model, Eq. (1), to the experimental trajectories. The initial positions and velocities were chosen to be the same as in the experiments. For each event, the experimental relative separation in time and the center-of-mass position in time were fitted to the corresponding trajectories obtained by numerical integration of the model equations. The fitting parameters were chosen to be radii for the two droplets and the product of their charges. We assumed that the droplet sizes did not vary significantly within a measurement so that there are only two radii parameters per measurement. This claim is backed up by our observations. Thus, during fitting, multiple events within the same measurement were simultaneously fitted assuming the droplet radii were the same for all events. The reason for fitting products of droplet charges is that this is the relevant parameter determining the Coulomb force. We fitted a different value of this product per event, to account for uncertainty and systematic errors in droplet charge measurements. Thus, for n fitted events, the number of fitting parameters was $n + 2$. The trajectories were fitted from the moment when the center-to-center droplet separation was $6(a_1 + a_2)$, up until they reached a separation of $2(a_1 + a_2)$ for the first time, or until they were last observed together.

F. Fixed-point analysis

Relative droplet dynamics takes place in nine dimensions: the separation \mathbf{R} , the relative velocity $\Delta \mathbf{v} = \mathbf{v}^{(2)} - \mathbf{v}^{(1)}$, and $\mathbf{v}^{(1)}$. The separation \mathbf{R} obeys the equation of motion

$$\dot{\mathbf{R}} = \Delta \mathbf{v}, \quad \Delta \dot{\mathbf{v}} = \frac{m_1 + m_2}{m_1 m_2} \frac{k_e q_1 q_2}{R^3} \mathbf{R} + \frac{\mathbf{F}_h^{(2)}}{m_2} - \frac{\mathbf{F}_h^{(1)}}{m_1}. \quad (4)$$

To characterize the droplet dynamics, we searched for fixed points of this dynamical system and analyzed their stability. The fixed-point conditions are $\dot{\mathbf{R}} = 0$ (constant droplet separation at saddle

TABLE I. Table comparing fitted charges and radii to experimentally reported values. The first column shows the measurements and the numbered events within each measurement (arbitrary indexing for events). Bold corresponds to a colliding trajectory while italic corresponds to a noncolliding one. Normal typeface corresponds to an inconclusive trajectory (see Sec. III C). The second column shows the fitted droplet radii with the experimentally reported radii in parentheses. The third column shows the squares of fitted charges (in units of 10^{-9} elementary charges squared), with the corresponding reported values in parentheses. The measurements 2018_07_25_measure_00_collision_08 and 2018_07_26_measure_00_collision_03 correspond to the events plotted in Fig. 1(a) and Figs. 1(b), 1(c), respectively, in the main text.

Measurement	Radius fitted (reported) (μm)	Charge fitted (reported) ($\frac{q_1 q_2}{e^2} 10^{-9}$)
2018_07_25_measure_00_collision_08		(0.0037 \pm 0.003)
494		
487		
489		
475	20.5 (21.3 \pm 2.0)	
483	24.4 (25.2 \pm 2.5)	
480		
492		
497		
2018_07_26_measure_00_collision_03		(-4.1 \pm 2.7)
390		-3.4388
392		-3.4652
393		-3.3997
395	19.5 (20.0 \pm 2.0)	-3.4035
402	23.7 (24.2 \pm 2.4)	-3.3148
394		-3.3662
386		-3.0987
403		-3.4289
2018_07_26_measure_00_collision_04		(-4.0 \pm 2.6)
347		-2.5983
352		-2.6106
357		-2.4186
362	20.4 (20.6 \pm 2.1)	-2.4534
367	24.4 (24.0 \pm 2.4)	-2.2638
372		-2.2688
377		-2.4077
2018_07_26_measure_00_collision_02		(-4.1 \pm 2.8)
405		-2.8858
408		-3.1250
411		-2.9430
414	20.0 (20.3 \pm 2.0)	-2.9892
417	23.7 (24.0 \pm 2.4)	-2.7313
420		-2.8954
423		-2.9454
426		-2.2981
406		-2.9431
2018_07_26_measure_00_collision_00		(-3.6 \pm 2.4)
446		-3.5093
447		-3.3692
449	20.3 (20.3 \pm 2.0)	-3.3110
450	23.4 (23.0 \pm 2.3)	-3.4071
451		-3.2807
452		-3.5480

TABLE I. (*Continued*).

Measurement	Radius fitted (reported) (μm)	Charge fitted (reported) ($\frac{q_1 q_2}{e^2} 10^{-9}$)
2018_08_06_measure_01_collision_02		(-9.7 ± 4.2)
1042		-5.8879
1043		-6.2777
1044	24.1 (23.8 ± 2.4)	-6.0872
1048	26.1 (25.0 ± 2.5)	-6.3287
1049		-5.6761
1050		-5.7901

point) as well as $\dot{\mathbf{v}}^{(j)} = 0$ for $j = 1, 2$. The last two equations yield the conditions

$$g - \frac{k_e}{m_1} \frac{q_1 q_2}{(\Delta y^*)^2} - 6\pi \mu a_1 \left(1 + \frac{3a_1 v_y^*}{8\nu}\right) \frac{v_y^*}{m_1} + 9\pi \mu a_1 a_2 \left(1 + \frac{3a_1 v_y^*}{8\nu}\right) \frac{v_y^*}{m_1} \frac{1}{\Delta y^*} = 0, \quad (5a)$$

$$g + \frac{k_e}{m_2} \frac{q_1 q_2}{(\Delta y^*)^2} - \frac{1}{m_2} 6\pi \mu a_2 \left(1 + \frac{3a_2 v_y^*}{8\nu}\right) \left[v_y^* + \left(e^{-\frac{\Delta y^* v_y^*}{\nu}} - 1 \right) \frac{3}{2} \frac{a_1 \nu}{\Delta y^*} \right] = 0. \quad (5b)$$

Equations (5) must be solved simultaneously for the fixed-point coordinates $\mathbf{v}^{(1)*} = (0, v_y^*, 0)$ and $\mathbf{R}^* = (0, \Delta y^*, 0)$. Note that the history force does not appear in Eqs. (5) because the droplets experience no acceleration at the saddle point. In summary, at the fixed point the droplets fall together at fixed separation Δy^* with the common velocity v_y^* . Analysis of the dynamics in the vicinity of the fixed point [Fig. 1(b)] shows that it is a saddle point [32].

Next we describe the dynamics close to the fixed points at infinity. When the droplets are infinitely far apart, they settle at their respective settling velocities. There is a fixed point of the relative droplet dynamics when $\Delta y = \pm\infty$. But how do the dynamics change when the droplets are at a large but finite separation? At a large separation, $\Delta \dot{y} = \Delta v_y < 0$ in our convention. Thus, Δy decreases from a large separation so that if $\Delta y > 0$ the system moves away from the fixed point but if $\Delta y < 0$ the system moves towards the fixed point at infinite separation. Thus, the fixed points at infinite separation are unstable when $\Delta y > 0$, but stable when $\Delta y < 0$.

For oppositely charged droplets, the larger droplet encounters the saddle point below the smaller one [red crosses in Figs. 1(b) and 1(c)]. The stable manifold of the saddle point connects to an unstable fixed point at infinity, where the droplets fall at their independent settling velocities [blue cross in Fig. 1(c)]. There is a continuum of such unstable fixed points, but only one connects to the saddle point. The connecting invariant manifold between the fixed points forms a separatrix that separates trajectories with qualitatively different behaviors [32].

IV. RESULTS

Consider first the dynamics of neutral droplets. Figure 1(a) compares measured spatial separations with numerical model trajectories. We see that the model works reasonably well, although the fits become worse for separations smaller than $2(a_1 + a_2)$. Noncolliding trajectories for which the particle separation remains large fit better than colliding ones. However, note that the noncolliding trajectory passing closest to the smaller droplet shows the largest deviation: while the experimental trajectory shows the larger droplet traveling at a fixed separation as it tumbles around the smaller one, the numerical model trajectory collides. The reason for this discrepancy is that the model does not contain higher-order corrections in a/R (lubrication forces [9]) needed at small separations. However, even with lubrication forces, the model cannot be used to compute collision efficiencies for neutral droplets, because they are determined by the breakdown of the hydrodynamic approximation below the mean free path [10] in the absence of charges.

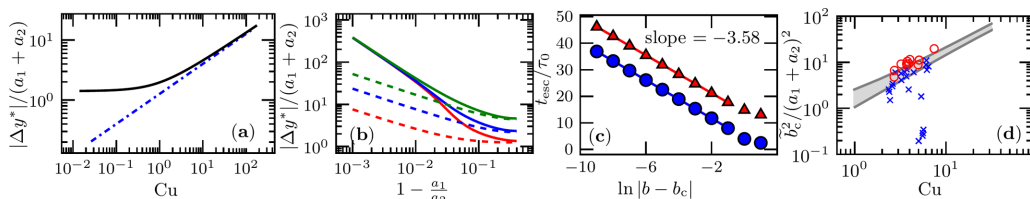


FIG. 2. (a) Location Δy^* of the fixed point in Fig. 1(b) as a function of Coulomb number Cu , for Eqs. (1) with $a_1/a_2 = 0.8$ (black), and without hydrodynamic interactions and without fluid inertia (blue, dash-dotted). (b) Δy^* as a function of droplet-radius ratio for different charges for the full model (solid), and excluding fluid inertia (dashed). Red, blue, and green correspond to charges of 6×10^3 , 6×10^4 and 3×10^5 elementary charges for one of the droplets, while the second droplets charge is kept fixed at 8.2×10^4 elementary charges. (c) Escape time t_{esc} normalized by the interaction timescale $\tau_0 = (a_1 + a_2)/|\Delta \mathbf{v}_0|$ plotted as a function of the difference of the impact parameter b from the critical impact parameter b_c , defined in the main text. Blue circles correspond to data points for which $b < b_c$, red triangles are for $b > b_c$. Red and blue lines show fitted exponential laws with slope -3.58 ± 0.02 . (d) Approximate collision efficiency using an approximate impact parameter \tilde{b}_c computed at the largest experimentally observed vertical separation, $\Delta y \approx 6(a_1 + a_2)$. Blue crosses and red circles correspond to experimentally observed collisions and misses, for the charged cases listed in Table I (the charges and droplet-radius ratios used to compute the Coulomb number for the experimental data are the fitted values given in Table I). Also shown are results of model calculations for radius ratio 0.8 (upper gray line) and 0.9 (lower gray line). See text for further details.

Relative trajectories of oppositely charged droplets are shown in Fig. 1(b). The electrical charges change the phase-space dynamics entirely, compared with the neutral droplets in Fig. 1(a). Now the larger droplet overtakes the smaller one before colliding [inset in panel (b)]. This cannot happen for neutral droplets, for which collisions always occur when the larger droplet is above the smaller one. The experimental trajectories suggest that the stable manifold of a saddle point forms a separatrix between the colliding and noncolliding trajectories. This is confirmed by the numerically simulated trajectories, where we fitted droplet charges in addition to droplet radii. The obtained charges were smaller than the experimental estimates, likely due to systematic errors in the experimental charge measurements, as discussed in Sec. III E above.

The corresponding relative velocities are shown in Fig. 1(c). The model accurately captures the observed relative velocities. We see that the relative speeds of the droplets decrease as they approach, dissipated by hydrodynamic interactions. All relative trajectories start close to an unstable fixed point where the droplets are infinitely far apart. At long times they either end up colliding, or converge to a stable fixed point where the droplets settle independently.

In summary, Figs. 1(b) and 1(c) suggest that for oppositely charged droplets the stable manifold of a saddle point forms the separatrix which explains droplet-collision outcomes. In other words, its Δx coordinate approaches b_c as $\Delta y \rightarrow \infty$. Noncolliding trajectories converge to a stable fixed point at infinite separation. Colliding trajectories remain outside the circular region demarcated by the separatrix. By contrast, Fig. 1(a) shows that no such saddle point exists in the case of neutral droplets.

Figures 2(a) and 2(b) show how the location of the saddle point changes as the droplet charges and radius ratio are varied. In order to understand this dependence, we start by discussing the origin of the saddle point. The saddle point in Figs. 1(b) and 1(c) emerges because gravity and hydrodynamic forces in Eq. (4) break the rotational symmetry of the Coulomb problem. In the absence of these perturbations, the solutions are periodic orbits determined by the balance between the attractive Coulomb force and the repulsive centrifugal force [21]. The Coulomb number Cu determines the radius of these orbits, equal to $Cu(a_1 + a_2)$. In the presence of gravity and hydrodynamic effects, by contrast, the Coulomb force is balanced by hydrodynamic forces. Solving the

fixed-point condition, Eqs. (5a) and (5b), for v_y^* and Δy^* yields

$$|\Delta y^*|^2 = \frac{-k_e q_1 q_2 (m_1 + m_2)}{m_1 F_{h,y}^{(2)}(\Delta y^*, v_y^*) - m_2 F_{h,y}^{(1)}(\Delta y^*, v_y^*)}. \quad (6)$$

Asymptotic expressions for Δy^* can be obtained in the limit of large charge and when $a_1 \rightarrow a_2$. As the charge magnitude increases, so does Δy^* , while v_y^* asymptotes to a constant value. Consequently, at large charges the first three terms in Eq. (5a) are comparable while the last term vanishes. Similarly, the second term in square brackets in Eq. (5b) vanishes as well. As a result, $F_{h,y}^{(j)}$ in Eq. (6) becomes independent of Δy^* in this limit, and we obtain the asymptotic dependence $\Delta y^* \propto \sqrt{q_1 q_2} \propto \sqrt{\text{Cu}}$ as $\text{Cu} \rightarrow \infty$, for fixed a_1 and a_2 . This explains the model-simulation results shown in Fig. 2(a). It also explains why Δy^* becomes independent of hydrodynamic interactions and fluid inertia at large Cu [Fig. 2(a)]: the corresponding terms in $F_{h,y}^{(1,2)}$ vanish as $|\Delta y^*| \rightarrow \infty$.

The situation is quite different for similarly sized droplets. Figure 2(b) indicates that fluid inertia causes $|\Delta y^*|$ to become insensitive to charge as $a_1 \rightarrow a_2$, and that fluid inertia plays a major role in this. When the droplets are far apart, Coulomb attraction ($\propto R^{-2}$) is negligible compared to attraction by fluid inertia ($\propto R^{-1}$). In the limit $a_1 \rightarrow a_2$, Δy^* diverges and one can ignore the Coulomb terms in Eqs. (5a) and (5b), as well as the exponential term in Eq. (5b), while the other terms remain of comparable magnitude. Solving for Δy^* , we find $|\Delta y^*| \sim |a_2 - a_1|^{-1}$ as $a_1 \rightarrow a_2$. As $|\Delta y^*|$ diverges, so does b_c : droplets always collide in this limit.

Droplet motion close to the saddle point is governed by the linearized dynamics. Figure 2(c) shows the time t_{esc} a droplet takes to pass close to the saddle point and reach a distance of $a_1 + a_2$ from it. The linear stability matrix at the saddle point determines the time t_{esc} which diverges as $t_{\text{esc}} \sim -\frac{1}{\lambda_+} \ln |b - b_c|$, where λ_+ is the leading eigenvalue of the stability matrix [32]. The stability of the saddle point (ignoring the history force) can be determined by calculating the eigenvalues, λ_i , $i = 1, \dots, 9$, of the Jacobian at the saddle point. Numerical diagonalization gives one eigenvalue with a positive real part and eight eigenvalues with negative real parts, $\text{Real}(\lambda_1) > 0 > \text{Real}(\lambda_2) \geq \text{Real}(\lambda_3) \geq \dots \geq \text{Real}(\lambda_9)$. The eigenvalue with positive real part corresponds to an eigenvector directed along the positive Δy and Δv_y directions. Numerical computation for typical experimental parameters [$a_1 = 19.5 \mu\text{m}$, $a_2 = 23.7 \mu\text{m}$, $q_1 = 6.5 \times 10^{-15} \text{ C}$ (41 000 elementary charges), and $q_2 = -1.2 \times 10^{-14} \text{ C}$ (74 000 elementary charges)] gives $\text{Real}(\lambda_1) = 139.9/\text{second}$. Normalizing this by the interaction time $\tau_0 = \frac{a_1 + a_2}{|\Delta v_0|}$ based on the initial relative velocity of the droplets gives $\lambda_+^{-1} = 3.46$, in good agreement with the scaling exponent for t_{esc} obtained from integrating model trajectories, shown in Fig. 2(c). The figure demonstrates that simulations of the escape time, including the history force, give a scaling $t_{\text{esc}} \sim -3.58 \ln |b - b_c|$. We expect that the reason for the good agreement is that the history force is a small correction, which does not drastically modify the escape time.

Figure 2(d) shows that our model explains the decision boundary between experimental droplet collisions and misses, for all charged events considered. The experimental data plotted corresponds to radius ratios between 0.82 and 0.87, except for one dataset (measurement 2018_08_06_measure_01_collision_02 in Table I) where $a_1/a_2 \approx 0.92$. The charges and radius ratios used to compute the Coulomb number for the experimental data are the fitted values given in Table I. Also shown are results of model calculations for an approximate collision efficiency, based on an approximate impact parameter that was evaluated at the largest experimentally observed droplet separations. Since the radius ratios vary in the experimental data, we plotted two model results, for $a_1/a_2 = 0.8$ (upper curve), and for $a_1/a_2 = 0.9$ (lower curve). The gray-shaded region predicts qualitatively correctly where the boundary between hits and misses occurs.

V. DISCUSSION

The stable manifolds of the saddle point shown in Figs. 2(b) and 2(c) prohibit the trajectories in the colliding region (blue trajectories) from escaping, so that they must collide. Further, for the

charges considered, the droplet separation at the saddle point and along its stable manifolds remains large enough so that they are not influenced by lubrication effects. Yet, as discussed in Sec. III D, our model is valid only when the droplet separation is large compared to their radius, for small values of a/R , and must fail when the droplet separation becomes small as for the colliding trajectories. What happens at these small separations, when the interfacial distances $s \ll a$? Consider first how the hydrodynamic interactions compete with the Coulomb force in this limit. At small s , the leading-order electrostatic force for two equally sized droplets (with radius a and mass m) is $F_e = -k_e(q_1 - q_2)^2[2as(\ln \frac{4a}{s})^2]^{-1}$ [34]. Also the leading-order hydrodynamic interaction (the lubrication force) diverges, as $-6\pi\mu a^2\Delta v/s$ [9]. Adding Coulomb interactions to the small- s equation of motion from Ref. [10] we find

$$\dot{s} = \Delta v, \quad (7a)$$

$$\frac{m}{2}\Delta\dot{v} = -6\pi\mu a^2\frac{\Delta v}{s} - \frac{k_e(q_1 - q_2)^2}{2as(\ln \frac{4a}{s})^2}. \quad (7b)$$

In the limit $s \rightarrow 0$, Eq. (7b) becomes overdamped, so that the relative velocity is given by

$$\Delta v = -\frac{k_e(q_1 - q_2)^2}{12\pi\mu a^3} \frac{1}{(\ln \frac{4a}{s})^2}. \quad (8)$$

This equation implies that the droplets collide in finite time because the electrostatic forces overpower the lubrication forces. Note that while this analysis applies to equally sized droplets, the qualitative conclusion remains the same for droplets with radius ratio close to unity. Also, the divergence of the lubrication force at small s is cut off by the breakdown of hydrodynamics at distances smaller than the mean free path [10]. This does not change the conclusion, because it tends to weaken the effect of hydrodynamic interactions. In summary, the Coulomb force dominates at small separations s ; neither lubrication forces nor their regularization by the breakdown of hydrodynamics make a difference.

For neutral droplets, by contrast, the breakdown of hydrodynamics is essential for droplet collisions, and the collision efficiency depends on Kn [10,35]. This limit is not obtained from our simplified model which must fail when the interfacial distance s at the fixed point, or at any point along the separatrix, becomes of the order of the mean free path. This is not the case when the droplet charge is large enough, as in the experimental data considered here, but might happen at smaller charges.

VI. CONCLUSIONS

We explained the qualitative nature of the collision dynamics of oppositely charged droplets settling in still air, and determined its parameter dependence by analyzing its fixed points, their stability, and their invariant manifolds. We found that a manifold connecting a saddle and an unstable fixed point separates colliding trajectories from noncolliding ones. Our analysis determines how Coulomb forces compete with inertial and hydrodynamic forces to determine the collision dynamics, and predicts how the collision efficiency of charged droplets settling in quiescent air depends on their charges. These main conclusions of our analysis are in good agreement with the experimentally observed collision dynamics of highly charged droplets, at high Coulomb number Cu . Our analysis allowed us to conclude that the collision efficiency of highly charged droplets does not depend on the Knudsen number, because the collision dynamics is determined by a separatrix along which the droplets are much further apart than the mean free path, for large Cu .

At smaller values of Cu , the saddle point may occur when the droplets are very close. When their interfacial distance at the saddle point (or on any point on the separatrix) is of the order of the mean free path, the collision efficiency is expected to depend on Kn. In order to determine a critical Coulomb number where the breakdown of hydrodynamics becomes important, one needs to consider higher-order corrections in a/R —not only to the electrostatic force, but also to the

hydrodynamic interactions (lubrication force)—and one must take into account the regularization of the lubrication force at interfacial distances smaller than the mean free path. In this limit, the precise location of the separatrix is surely affected by how noncontinuum effects regularize lubrication forces. While it is a challenge to find reliable approximations when the droplets are close, we nevertheless expect that the fixed-point analysis described in this paper will enable progress. Since the collision dynamics is discontinuous, bifurcation mechanisms observed in nonsmooth dynamical systems [36] may become important.

In our manuscript, we considered the significance of the parameters C_u and Kn . For the remaining dimensionless parameters (the radius ratio, Stokes number, particle Reynolds number, and Strouhal number), we assumed values characteristic for the experiment. Preliminary model simulations suggest that the collision dynamics is not sensitive to changes in these dimensionless parameters, at least in the parameter range considered here. We leave a detailed study of these effects to future work.

Concerning droplet growth by collision and coalescence, note that collision kernels depend not only upon the critical impact parameter but also on relative velocities [37]. Since this velocity vanishes at the saddle point, droplets may collide at smaller relative velocities compared to neutral droplets, at least at small charges where the saddle point occurs for nearby droplets. This could give weakly charged droplets more time to interact.

While our charges are considerably smaller than those in the innovative study of spatial droplet patterns in turbulence [23–25], they are nevertheless larger than the charges in warm clouds by about one order of magnitude [38]. To validate models for the dynamics of closely approaching droplets, measurements for weakly charged droplets are necessary.

Updrafts in clouds cause air turbulence which may affect the cloud-droplet collisions [39]. Turbulent strains increase the collision rate of very small, neutral droplets [40]. Recent numerical simulations of droplet collisions in a straining flow exhibit a rich variety of different dynamical behavior in this regime, as well as intricate parameter dependencies [35]. For larger Stokes numbers, as in the present paper, the effect of particle inertia can significantly enhance the Saffman-Turner collision rate [41–43]. It remains an open question how turbulence competes with the collision mechanisms studied in the present paper.

Lu *et al.* [23,24] and Lu and Shaw [25] measured the effect of electrostatic charges on the spatial distribution of droplets in turbulence on scales much larger than the droplet size. Little is known about the effect on smaller spatial scales, where hydrodynamic interactions must begin to matter. How does the spatial clustering observed by Lu *et al.* develop as the charges become smaller? This is a challenging question, not least because recent experiments [44,45] suggest evidence for extreme spatial clustering of small droplets in turbulence, which remains to be understood.

Finally, an important open question concerns the fluctuations of relative velocities of weakly charged droplets in turbulence. The phase-space dynamics in the presence of an external flow is expected to be quite different from that shown in Figs. 1(b) and 1(c), but we expect that a systematic bifurcation analysis will reveal the underlying mechanisms, at least for steady flows.

ACKNOWLEDGMENTS

This work was supported by the National Science Foundation under Grant No. CBET-1605195. The research of B.M. and A.D. was supported by a grant from Vetenskapsrådet (Grant No. 2017-3865) and from the Knut and Alice Wallenberg Foundation (Grant No. 2014.0048). Computational resources were provided by C3SE and SNIC. This work was concluded while B.M. was supported by a Mary Shepard B. Upson Visiting Professorship at Cornell University.

APPENDIX A: EXPERIMENTAL SETUP

We analyzed collisions between pairs of droplets approaching each other in still air using data that was obtained with a set up developed by Hanstorp *et al.* [19] and Ivanov *et al.* [46].

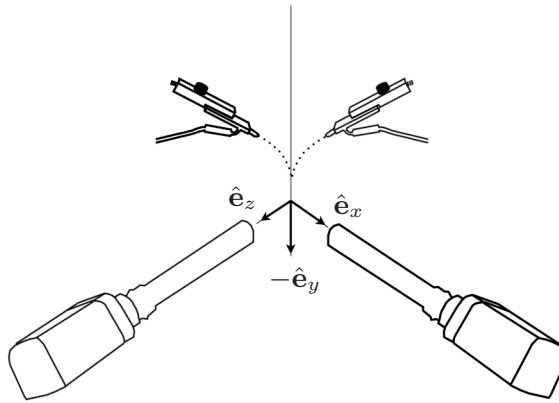


FIG. 3. Experimental setup. Shown are the two droplet dispensers (top), the two cameras at right angles (bottom), and two droplets paths. The axes of the cameras are parallel with the x and z axes.

Droplets were generated using inkjet-printer technology as described by Sergeyev and Shaw [26]. Two printer nozzles were angled at each other such that collisions and near-collisions occurred in the observation volume where the fields of view of two high-speed cameras (Phantom Miro Lab310 from Vision Research) were aligned. Optical traps [19] were not used. We defined the laboratory-frame coordinates to be collinear with the axes of the cameras, so that one camera pointed along the z axis (viewing images in the x - y plane), and the other was aligned with the x axis (viewing images in the y - z plane). Gravity pointed in the negative y direction to within 3° . The setup is shown schematically in Fig. 3. The cameras were equipped with long distance microscopes (Model K2 DistaMax from Infinity) so that the droplet images were magnified by about 11 times. The resolution of each camera was measured by taking a picture of a flat calibration mask (Thorlabs model R2L2S3P1). The spatial resolution of each camera was found to be 1.78 and 1.70 $\mu\text{m}/\text{pixel}$. The uncertainty in the resolution is $\pm 10\%$ [46].

The droplet generators were triggered such that pairs of droplets were generated one after another. This allowed between 1 and 40 approaching droplet pairs to be recorded in the same measurement before the memory of the cameras filled up. The droplet pairs were generated slowly enough that no more than two droplets were in the observation volume at once. Charge was imparted to the droplets by applying a DC voltage to an electrode near the dispenser nozzle as in Hanstorp *et al.* [19]. Each measurement was stored in the Phantom camera .cine format, which includes both the image data and metadata such as date of collection and frame rate. The data files are labeled as follows: YYYY_MM_DD_measure_XX_collision_XX. Here, YYYY_MM_DD refers to the date on which the measurement was performed. The numbers following measure and collision are labels for different measurements. The sampling rate of the cameras were set to either 8500 or 25 000 frames per second, depending on the experiment.

A total of 1291 droplet pairs were observed, with radii between 20 and 26 μm (see Table I) and impact parameters b between about 0.1 and 6. As explained in the main text, this approximate impact parameter was computed at the observed initial separation of the droplets, which varied between $2(a_1 + a_2)$ and $6(a_1 + a_2)$. In the absence of external forces, it is equal to 0 when the droplets approach each other head on, and approximately 1 during a grazing collision where the droplets touch edges with the relative velocity perpendicular to the separation vector. The impact parameter varied from event to event because of randomness in the droplet generation process, and it varied between different sets of experimental conditions because of changes to the droplet generators' positions and angles. The initial velocity of the droplets could be controlled by changing the signal sent to the droplet generators, but this signal was not altered during the experiments. In this Appendix and in Appendix B, we describe all available data collected, although not all data are

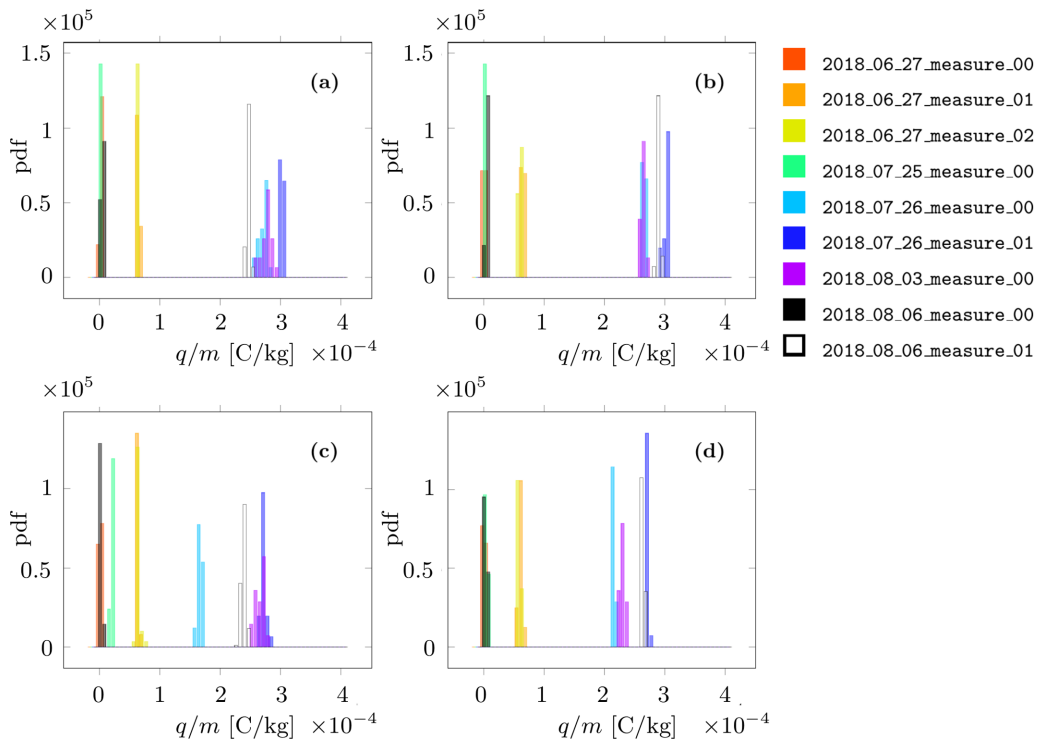


FIG. 4. Estimated droplet charge-per-mass ratios. (a) Primary droplet, before the data were collected. (b) Satellite droplet, before the data were collected. (c) Primary droplet, after the data were collected. (d) Satellite droplet, after the data were collected. The color of each distribution indicates the name of the measurement according to the legend.

used in the main paper. Two video recordings of representative near-contact events are included as Supplemental Material [33].

The charge-per-mass ratio was measured before and after data collection by allowing single droplets to fall between two parallel capacitor plates, where each trajectory was observed by a web camera with a large field of view so that the full path of the droplet between the plates could be observed [19]. The linear size of the plates was much larger than that of the region of observation, so it can be assumed that the electric field was homogeneous. The voltage on the charging electrode was changed manually until the desired deflection of the droplet path was achieved for each of the two dispensers. To determine the direction of gravity, the single droplets were first observed falling without any voltage applied.

The deflection angle α of the settling path due to charge on the plates was used to calculate the charge per mass by

$$\frac{q}{m} = \frac{gd}{U} \tan \alpha, \quad (\text{A1})$$

where g is the acceleration due to gravity, d is the separation distance between the plates ($d = 17$ mm), and U is the applied voltage difference across the plates (which was set to 100 V). The distribution of q/m estimated from Eq. (A1) for each set of data is shown in Fig. 4. We refer to the smaller droplet in each pair as the primary droplet and the larger droplet as the satellite droplet. The charge-to-mass ratio varies between 1×10^{-6} and 3×10^{-3} C/kg.

The variation in charge-to-mass ratio before and after data collection for each measurement was within 5×10^{-5} C/kg except for the measurement 2018_07_26_measure_00 wherein it varied by

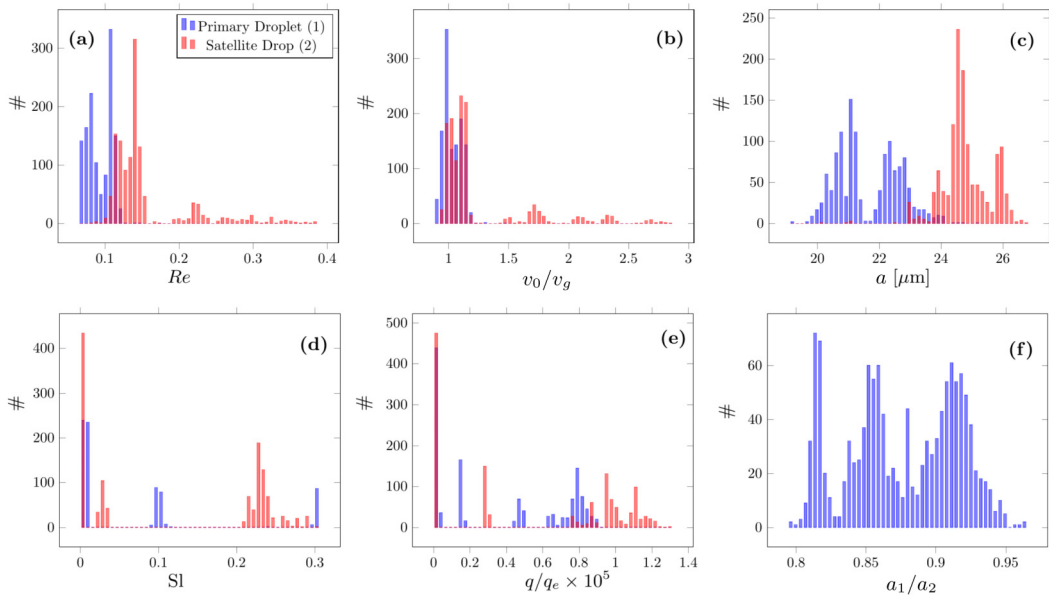


FIG. 5. Distribution of estimated parameters. (a) Distribution of droplet-Reynolds numbers. (b) Distribution of initial speeds divided by the Stokes terminal velocity v_g . (c) Distribution of droplet radii. (d) Distribution of the droplet-Strouhal number. (e) Distribution of droplet charges in number of electrons. (f) Distribution of radius ratio between primary and satellite droplet.

1×10^{-4} C/kg for the primary droplet. The large shift in the distribution of charge-to-mass ratio in Fig. 4 from before to after data collection was most likely due to misalignment between the axis of the web camera and the direction of gravity; an upward or downward tilt of the camera would tend to cause an overestimate of the deflection angle. Additionally, it was necessary to clean the dispenser nozzles at regular intervals to prevent clogging, which may have altered the charge imparted to the droplets.

APPENDIX B: RANGE OF PARAMETERS STUDIED

Figure 5 shows a summary of some important droplet characteristics. Droplet Reynolds numbers are shown in Fig. 5(a). We define $Re_p = \frac{av}{\nu}$ as in the main text, where a is the droplet radius, v is the average speed of the droplet over the entire time it is observed, and $\nu = 1.48 \times 10^{-5}$ m²/s is the kinematic viscosity of air. The data where the satellite droplet achieved $Re_p > 0.2$ are from 2018_06_20 and 2018_06_27. In these events, the satellite droplets had initial velocities that were large compared to their Stokes settling speed because they retained momentum from their emission from the droplet generator. In later measurements, the droplet generators were adjusted so the satellite droplets had more time to relax to their settling speed. The droplet Reynolds numbers were small but nonzero.

The ratios of the initial speed of the droplets v_0 to their Stokes settling speed v_g are shown in Fig. 5(b). The settling speed is calculated using $v_g = \frac{2}{9} \frac{\rho_p}{\rho_f} a^2 g$, where $\rho_p = 1000$ kg/m³ is the mass density of water, $\rho_f = 1.23$ kg/m³ is the mass density of air, and $g = 9.81$ m/s² is the acceleration due to gravity. The initial speed of the droplets was of the same magnitude as the Stokes settling speed except for measurements performed on 2018_06_20 and 2018_06_27, where, as mentioned above, the satellite droplets had initial velocities that were large because they retained momentum from their emission from the droplet generator.

The measured droplet radii are shown in Fig. 5(c). An estimate for the droplet radius was measured at each time the cameras observed a droplet. As discussed in Sec. III B, we used only size estimates from camera 1 and applied a correction factor of 0.85 to map from the radius of the shadows cast by the droplets to their actual radii. The values shown here are the distribution of the 10th percentile from each droplet trajectory. The uncertainty in measuring the droplet radius from the particle identification algorithm is no more than half a pixel, which corresponds to about $0.9 \mu\text{m}$. The dominant source of uncertainty in measuring the radii comes from uncertainty in the spatial resolution, which is $\pm 10\%$.

The distribution of the Strouhal number, $St = a/(v\tau_c)$ is shown in panel (d). Here τ_c is the characteristic acceleration timescale due to electrical charges on the droplets, $\tau_c = \sqrt{a/a_c}$, where a_c is the Coulomb acceleration upon contact. The distributions show that the Strouhal number ranges up to 0.3.

The droplet charges are shown in panel (e). We estimated the charges using the average charge-per-mass for each measurement obtained from the calibration procedure (results shown in Fig. 4) and the mass of the droplets measured from their size assuming the density was 1000 kg/m^3 . The droplets in the present experiment carried between several hundred to about 10^5 elementary charges, either positive or negative. The oppositely charged droplets carried between 0.6×10^5 and 1.2×10^5 elementary charges; see Table I. For comparison, $25 \mu\text{m}$ radius droplets in thunderstorm clouds carry an average charge of about 0.2×10^5 elementary charges while warm clouds can contain droplets with an average charge of about 0.2×10^4 elementary charges [38].

Most other studies considered much larger charges. Abbott [15] studied droplets settling in still air with 1×10^6 to 8×10^6 elementary charges (near $1 \times 10^{-5} \text{ C/m}^2$). Lu *et al.* [23–25] measured how charges affect spatial clustering of particles in turbulence. Their droplets carried from 3×10^5 to 4×10^5 elementary charges. The maximum charge a droplet can contain before electrostatic forces overwhelm surface tension and the droplet bursts is given by $q^2 = 64\pi^2\epsilon_0\gamma a^3$ [47], where q is the maximum charge the droplet can sustain, ϵ_0 is the permittivity of free space, and γ is the surface tension of the droplet. For a droplet with a radius of $20 \mu\text{m}$, for example, the maximum charge it can contain is about 10^7 elementary charges. The charges in this experiment are well below this limit.

Uncertainty in estimating the charge on each droplet arises from uncertainty in the mass of the droplets, which is calculated from the measured radii, and from uncertainty in the charge per mass measured from the calibration procedure. For measurements with approximately uncharged droplets, uncertainty from the calibration procedure dominates; these droplets may contain between 0 and several thousand electrons. For measurements with highly charged droplets (excluding 2018_07_26_measure_00, discussed below), uncertainty in the mass of the droplets dominates; these droplets may contain $\pm 30\%$ the number of electrons indicated in Fig. 5(e). As discussed in Appendix A, the uncertainty in measuring the charge-per-mass of the droplets in the measurement 2018_07_26_measure_00 was substantially larger, so both uncertainty in the mass of the droplets and uncertainty in the charge per mass play a role in the total uncertainty. For this measurement only, the uncertainty in charge contained on the droplets is $\pm 56\%$ for the primary droplet and $\pm 37\%$ for the satellite droplet. The distribution of ratio of primary droplet radius to satellite droplet radius is shown in Fig. 5(f).

-
- [1] H. R. Pruppacher and J. D. Klett, *Microphysics of Clouds and Precipitation* (Springer, Dordrecht, 2010).
 - [2] R. G. Harrison, K. A. Nicoll, and M. H. P. Ambaum, On the microphysical effects of observed cloud edge charging, *Q. J. R. Meteorol. Soc.* **141**, 2690 (2015).
 - [3] K. Gustavsson and B. Mehlh, Statistical models for spatial patterns of heavy particles in turbulence, *Adv. Phys.* **65**, 1 (2016).

- [4] M. A. Rother, J. K. Stark, and R. H. Davis, Gravitational collision efficiencies of small viscous drops at finite Stokes numbers and low Reynolds numbers, *Int. J. Multiphase Flow* **146**, 103876 (2022).
- [5] J. D. Klett and M. H. Davis, Theoretical collision efficiencies of cloud droplets at small Reynolds numbers, *J. Atmos. Sci.* **30**, 107 (1973).
- [6] C. E. Abbott, Experimental cloud droplet collection efficiencies, *J. Geophys. Res.* **79**, 3098 (1974).
- [7] J. D. Sartor, Comment on ‘Experimental cloud droplet collection efficiencies’ by C. E. Abbott, *J. Geophys. Res.* **80**, 1697 (1975).
- [8] J. D. Sartor, Comment on ‘Reply’ by C. E. Abbott, *J. Geophys. Res.* **80**, 3508 (1975).
- [9] S. Kim and S. J. Karrila, *Microhydrodynamics: Principles and Selected Applications* (Butterworth-Heinemann, Boston, 1991).
- [10] R. R. Sundararajakumar and D. L. Koch, Non-continuum lubrication flows between particles colliding in a gas, *J. Fluid Mech.* **313**, 283 (1996).
- [11] M. H. Davis, Two charged spherical conductors in a uniform electric field: Forces and field strength, *Q. J. Mech. Appl. Math.* **17**, 499 (1964).
- [12] B. A. Tinsley and L. Zhou, Comments on “Effect of electric charge on collisions between cloud droplets”, *J. Appl. Meteorol. Climatol.* **53**, 1317 (2014).
- [13] R. G. Semonin and H. R. Plumlee, Collision efficiency of charged cloud droplets in electric fields, *J. Geophys. Res.* **71**, 4271 (1966).
- [14] I. Paluch, Theoretical collision efficiencies of charged cloud droplets, *J. Geophys. Res.* **75**, 1633 (1970).
- [15] C. E. Abbott, Charged droplet collision efficiency measurements, *J. Appl. Meteorol.* **14**, 87 (1975).
- [16] R. J. Schlamp, S. N. Grover, H. R. Pruppacher, and A. E. Hamielec, A numerical investigation of the effect of electric charges and vertical external electric fields on the collision efficiency of cloud drops. *J. Atmos. Sci.* **33**, 1747 (1976).
- [17] R. J. Schlamp, S. N. Grover, H. R. Pruppacher, and A. E. Hamielec, A numerical investigation of the effect of electric charges and vertical external electric fields on the collision efficiency of cloud drops: Part II, *J. Atmos. Sci.* **36**, 339 (1979).
- [18] R. V. Kearney and G. P. Bewley, Lagrangian tracking of colliding droplets, *Exp. Fluids* **61**, 155 (2020).
- [19] D. Hanstorp, M. Ivanov, A. F. A. Hernandez, J. Enger, A. M. Gallego, O. Isaksson, C.J. Karlsson, R.M. Villa, A. Varghese, and K. Chang, *A versatile system for optical manipulation experiments*, in *Optical Trapping and Optical Micromanipulation XIV*, SPIE Proceedings Vol. 10347 (SPIE, Bellingham, WA, 2017), p. 103472C.
- [20] F. Candelier and B. Mehlig, Settling of an asymmetric dumbbell in a quiescent fluid, *J. Fluid Mech.* **802**, 174 (2016).
- [21] H. Goldstein, C. P. Poole, and J. L. Safko, *Classical Mechanics* (Addison Wesley, Reading, MA, 2002).
- [22] G. M. Hidy and J. R. Brock, Some remarks about the coagulation of aerosol particles by Brownian motion, *J. Colloid Sci.* **20**, 477 (1965).
- [23] J. Lu, H. Nordsiek, E.W. Saw, and R. A. Shaw, Clustering of Charged Inertial Particles in Turbulence, *Phys. Rev. Lett.* **104**, 184505 (2010).
- [24] J. Lu, H. Nordsiek, and R. A. Shaw, Clustering of settling charged particles in turbulence: theory and experiments, *New J. Phys.* **12**, 123030 (2010).
- [25] J. Lu and R. A. Shaw, Charged particle dynamics in turbulence: Theory and direct numerical simulations, *Phys. Fluids* **27**, 065111 (2015).
- [26] A.V. Sergeev and R. A. Shaw, An inexpensive uniform-size aerosol generator, *Meas. Sci. Technol.* **17**, N41 (2006).
- [27] V. Pratt, *Direct least-squares fitting of algebraic surfaces*, in *SIGGRAPH '87: Proceedings of the 14th Annual Conference on Computer graphics and Interactive Techniques*, August 1987 (ACM, New York, 1987), p. 145.

- [28] J. Einarsson, A. Johansson, S. K. Mahato, Y. N. Mishra, J. R. Angilella, D. Hanstorp, and B. Mehlig, Periodic and aperiodic tumbling of microrods advected in a microchannel flow, *Acta Mech.* **224**, 2281 (2013).
- [29] J. Qian and C. K. Law, Regimes of coalescence and separation in droplet collision, *J. Fluid Mech.* **331**, 59 (1997).
- [30] A. M. Ardekani and R. H. Rangel, Unsteady motion of two solid spheres in Stokes flow, *Phys. Fluids* **18**, 103306 (2006).
- [31] G. F. Carrier, On slow viscous flow, final report, Brown University, 1953 (unpublished).
- [32] S.H. Strogatz, *Nonlinear Dynamics and Chaos: With Applications to Physics, Biology, Chemistry and Engineering*, Studies in Nonlinearity (Westview, Boulder, CO, 2000).
- [33] See Supplemental Material at <http://link.aps.org/supplemental/10.1103/PhysRevFluids.7.043601> for two video recordings: one shows a near miss, while the other one shows a collision.
- [34] J. Lekner, Electrostatics of two charged conducting spheres, *Proc. R. Soc. A* **468**, 2829 (2012).
- [35] J. Dhanasekaran, A. Roy, and D. L. Koch, Collision rate of bidisperse spheres settling in a compressional non-continuum gas flow, *J. Fluid Mech.*, **910**, A10 (2021).
- [36] M. di Bernardo and S. J. Hogan, Discontinuity-induced bifurcations of piecewise smooth dynamical systems, *Philos. Trans. R. Soc. A* **368**, 4915 (2010).
- [37] K. Gustavsson and B. Mehlig, Relative velocities of inertial particles in turbulent aerosols, *J. Turbul.* **15**, 34 (2014).
- [38] T. Takahashi, Measurement of electric charge of cloud droplets, drizzle, and raindrops, *Rev. Geophys.* **11**, 903 (1973).
- [39] E. Bodenschatz, S.P. Malinowski, R.A. Shaw, and F. Stratman, *Science* **327**, 970 (2010).
- [40] P. G. Saffman and J. S. Turner, On the collision of drops in turbulent clouds, *J. Fluid Mech.* **1**, 16 (1956).
- [41] S. Sundaram and L. R. Collins, Collision statistics in an isotropic particle-laden turbulent suspension. Part 1. Direct numerical simulations, *J. Fluid Mech.* **335**, 75 (1997).
- [42] G. Falkovich, A. Fouxon, and G. Stepanov, Acceleration of rain initiation by cloud turbulence, *Nature (London)* **419**, 151 (2002).
- [43] M. Wilkinson, B. Mehlig, and V. Bezuglyy, Caustic Activation of Rain Showers, *Phys. Rev. Lett.* **97**, 048501 (2006).
- [44] M. A. Yavuz, R. P. J. Kunnen, G. J. F. van Heijst, and H. J. H. Clercx, Extreme Small-Scale Clustering of Droplets in Turbulence Driven by Hydrodynamic Interactions, *Phys. Rev. Lett.* **120**, 244504 (2018).
- [45] A. D. Bragg, A. L. Hammond, R. Dhariwal, and H. Meng, Hydrodynamic interactions and extreme particle clustering in turbulence, *J. Fluid Mech.* **933**, A31 (2022).
- [46] M. Ivanov, K. Chang, I. Galinskiy, B. Mehlig, and D. Hanstorp, Optical manipulation for studies of collisional dynamics of micron-sized droplets under gravity, *Opt. Express* **25**, 1391 (2017).
- [47] Lord Rayleigh, XX. On the equilibrium of liquid conducting masses charged with electricity, *London Edinburgh Dublin Philos. Mag. J. Sci.* **14**, 184 (1882).